nature communications

Article

https://doi.org/10.1038/s41467-024-52998-9

Cryo-EM investigation of ryanodine receptor type 3

Received: 30 May 2024

Accepted: 27 September 2024

Published online: 05 October 2024

Check for updates

Yu Seby Chen[1], Maricela Garcia-Castañeda[1], Maria Charalambous[1], Daniela Rossi[2], Vincenzo Sorrentino[2] & Filip Van Petegem[1]

Ryanodine Receptor isoform 3 (RyR3) is a large ion channel found in the endoplasmic reticulum membrane of many different cell types. Within the hippocampal region of the brain, it is found in dendritic spines and regulates synaptic plasticity. It controls myogenic tone in arteries and is upregulated in skeletal muscle in early development. RyR3 has a unique functional profile with a very high sensitivity to activating ligands, enabling high gain in Ca^{2+}-induced Ca^{2+} release. Here we solve high-resolution cryo-EM structures of RyR3 in non-activating and activating conditions, revealing structural transitions that occur during channel opening. Addition of activating ligands yields only open channels, indicating an intrinsically high open probability under these conditions. RyR3 has reduced binding affinity to the auxiliary protein FKBP12.6 due to several sequence variations in the binding interface. We map disease-associated sequence variants and binding sites for known pharmacological agents. The N-terminal region contains ligand binding sites for a putative chloride anion and ATP, both of which are targeted by sequence variants linked to epileptic encephalopathy.

Ryanodine receptors (RyRs) are ion channels that release Ca^{2+} from the endoplasmic (ER) and sarcoplasmic reticulum (SR)[1]. With molecular weights >2 MDa, they are the largest ion channels currently known. Of the three isoforms (RyR1-3) that are found in mammals, the type 3 ryanodine receptor was first identified in mammalian brain[2], but has since been found in many different cell types[3].

Within the brain, RyR3 is primarily found in the hippocampus and striatum in adults[4–6]. Although RyR1 and RyR2 are also found throughout the central nervous system, RyR3 plays distinct roles[4,7]. For example, in primary hippocampal neurons, RyR3 is the only isoform found in dendritic spines[8]. Activated by increases in cytosolic Ca^{2+}, RyR3 likely amplifies Ca^{2+} signals originating from the plasma membrane at postsynaptic dendritic spines, which then propagate to the dendrite and activate RyR2, which is more prevalent in this region. Accordingly, RyR3 has been shown to play a role in learning and memory, as its knock-down or sheer knock-out leads to impaired spatial learning and neuronal plasticity[9,10], reduced social interactions and hyperactivity[11]. Its role in the brain is underscored by several disorders. RyR3 is overexpressed in hippocampal neurons of Alzheimer's disease mouse models[12,13], and its overexpression has also been associated with depression-like behavior[14].

Outside of the brain, RyR3 is found in multiple tissues with specifically assigned roles in tracheal epithelium[15], pre-adipocytes[16], cerebral arteries[17], but also in stomach, spleen, intestines, esophagus, kidneys and more[3]. Given this diverse array of cell types, single nucleotide polymorphisms in RyR3 have been associated with a range of traits and disorders, including plasma adiponectin levels[18], atherosclerosis[19–21], hypertension and diabetes[22], Alzheimer's[22], fetal akinesia[23], and neuroleptic malignant syndrome[24]. However, a direct causative link between RyR3 mutations and disease has not been proven to date.

Concomitant with a specialized role for RyR3, its intrinsic functional properties differ substantially from RyR1 and RyR2. Being the shortest of the three isoforms, it has a higher sensitivity to activating ligands like Ca^{2+} and caffeine, to oxidating conditions, and is characterized by a much higher maximum open probability[25–28]. This

[1]Department of Biochemistry and Molecular Biology, the Life Sciences Centre, University of British Columbia, Vancouver, BC, Canada. [2]Department of Molecular and Developmental Medicine, University of Siena, Siena, Italy. e-mail: filip.vanpetegem@ubc.ca

profile enables a specialized role in tissues where other isoforms are also expressed. In skeletal muscle, for example, RyR1 is the predominant isoform expressed in the SR membrane. This is easily understood, as RyR1 is mechanically coupled to L-type Ca^{2+} channels in the T-tubule membrane, whereas RyR3 is not, and this effect is due to specific sequence differences in distinct regions[29–31]. However, neonatal muscle lacks well-developed T-tubule systems, and are more reliant on Ca^{2+}-induced Ca^{2+} release (CICR), which is strongly amplified by RyR3 by virtue of its enhanced Ca^{2+} sensitivity[32]. The relative content of RyR3 in adults also varies substantially depending on the exact muscle, with much higher concentrations in diaphragm[33,34]. This is particularly the case in extraocular muscle, where RyR3 is abundant, and its deletion strongly affects the muscle mechanical properties and vision[35]. In accordance with its role in skeletal muscle, RyR3 sequence variants have been associated with nemaline myopathy[36].

High-resolution insights into RyR3 structure have been limited, with a crystal structure available for the individual Repeat3&4 domain[37], and unpublished structures of the Repeat1&2 domain (PDB entries 6UHA, 6UHB, 6UHE, 6UHH). Previous cryo-EM studies on full-length RyR3 have been limited to very low resolutions ~30–40 Å[38,39], thus not allowing any atomic-level interpretation.

Here we present high-resolution cryo-EM structures of recombinantly expressed mammalian RyR3. Our structural studies reveal a channel with a high intrinsic open probability, a distinct profile for binding small molecule ligands and altered interfaces for binding auxiliary proteins like FKBP12.6.

Results

Structures of RyR3 in non-activating and activating conditions

We purified mink RyR3, recombinantly expressed in stable HEK293 cells, and determined cryo-EM structures in two conditions: non-activating (5 mM EGTA) and activating (30 μM free Ca^{2+}, 5 mM ATP, and 5 mM caffeine). These led to reconstructions at 2.89 and 3.22 Å global resolution, respectively (Fig. 1; Supplementary Fig. 1 and 2; Supplementary Table 1). In both cases, FKBP12.6 was utilized to purify the channel, and was therefore present in the final reconstructions. To determine the state of the pore in both conditions (open versus closed), we used classification on a masked transmembrane region and found that the non-activating condition gave rise to a homogeneous population of particles with only closed pores. Conversely, the activating conditions only yielded open channels. This is in contrast with RyR1 and RyR2, where similar activating conditions typically yield a mixture of open and closed channels[1,40,41]. This indicates an increased sensitivity of RyR3 for activating conditions and is in line with functional data, which have shown a higher open probability of RyR3 compared to the other isoforms[25–28]. Using symmetry expansion and masked refinement, we highly improved the local resolution for individual regions, yielding local resolutions in the pore domain of 2.6 and 2.8 Å for non-activating and activating conditions, respectively. The poorest resolution was obtained for the Repeat1&2 domain (~6 Å) and the Repeat3&4 domain (nearly invisible), indicating high relative flexibility for these domains (Fig. 1a, b; Supplementary Figs. 1 and 2). An overview of the various domains is shown in Fig. 1c, d.

Conformational changes in cytosolic domains upon channel opening

Upon channel opening, the large cytosolic cap of RyR3 undergoes large outward and downward motions away from the central fourfold symmetry axis (Fig. 2a; Supplementary Movie 1). These involve concerted movements in the N-terminal, Nsol, SPRY, Jsol, Bsol, Csol, and C-terminal domains. Consequently, modulatory ligands or proteins that induce conformational changes in any of these cytosolic domains will likely also affect channel gating.

Between the closed and open states, the Bsol domain shows the largest downward movements (~10 Å) at the periphery (Fig. 2b). Of note, a pocket within the Bsol contains additional density not observed in previous high-resolution structures of RyR1[42] or RyR2[41]. We attribute this density to a loop further downstream in the Bsol sequence. The contacts are mediated by Arg3384 within the loop and by Trp2513, Cys2517, His2872, and Asn2871 in the pocket.

Closer to the fourfold symmetry axis, the N-terminal domains (NTD-A and NTD-B) from all four subunits form a near continuous ring, with NTD-A of one subunit being juxtaposed to NTD-B′ of a neighboring subunit (Fig. 2c–f). Direct interactions may exist between Lys157 and Gln158 of NTD-A and Asp231′ and His230′ of NTD-B′, but the side chain density for Lys157 and Gln158 is poorly resolved, and thus such interactions are, at most, transient. In the open state, however, the gap between NTD-A and NTD-B′ across subunits widens substantially, with a relative movement of ~4.5 Å measured by the increase in Cα-Cα distances between Lys157 and His230′. In contrast, the

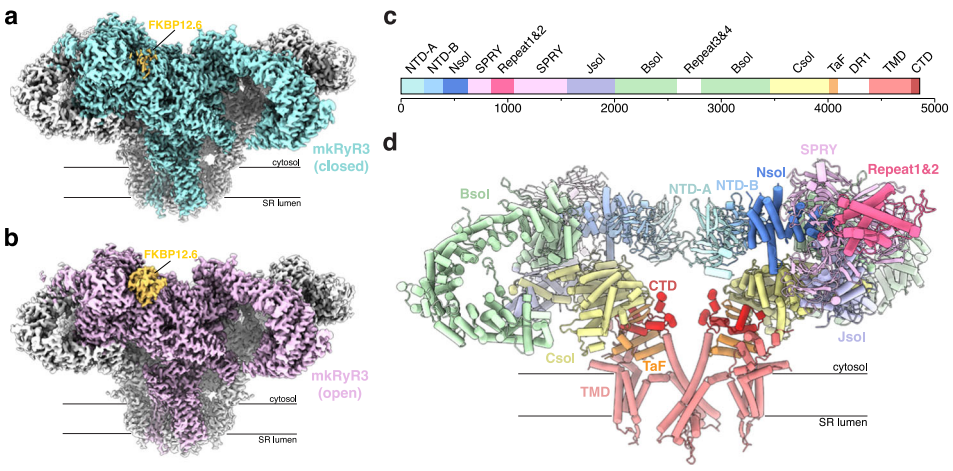

Fig. 1 | Cryo-EM structures of RyR3 in absence and presence of activating ligands. a Composite map of RyR3 in closed conformation determined in presence of 5 mM EGTA. One subunit of RyR3 (*cyan*) and FKBP12.6 (*yellow*) are colored. Map contour level = 0.21. **b** Composite map of RyR3 in open conformation determined in presence of activating ligands (5 mM ATP, 5 mM caffeine, and 30 μM free Ca^{2+}). One subunit of RyR3 (*pink*) and FKBP12.6 (*yellow*) are colored. Map contour level = 0.20. **c** Domain organization of RyR3. NTD-A and NTD-B, NH_2-terminal domains A and B, Nsol NH_2-terminal solenoid domain, SPRY SPRY domains 1-3, Jsol junctional solenoid domain, Bsol bridging solenoid domain, Csol central solenoid domain, TaF thumb-and-forefinger domain, DR1 divergent region 1, TMD transmembrane domain, CTD COOH-terminal domain. See Supplementary Table 2 for domain boundaries. **d** Structure of closed state RyR3 viewed from the membrane plane. Only two out of four subunits are shown. The domains are colored according to (**c**).

https://doi.org/10.1038/s41467-024-52998-9

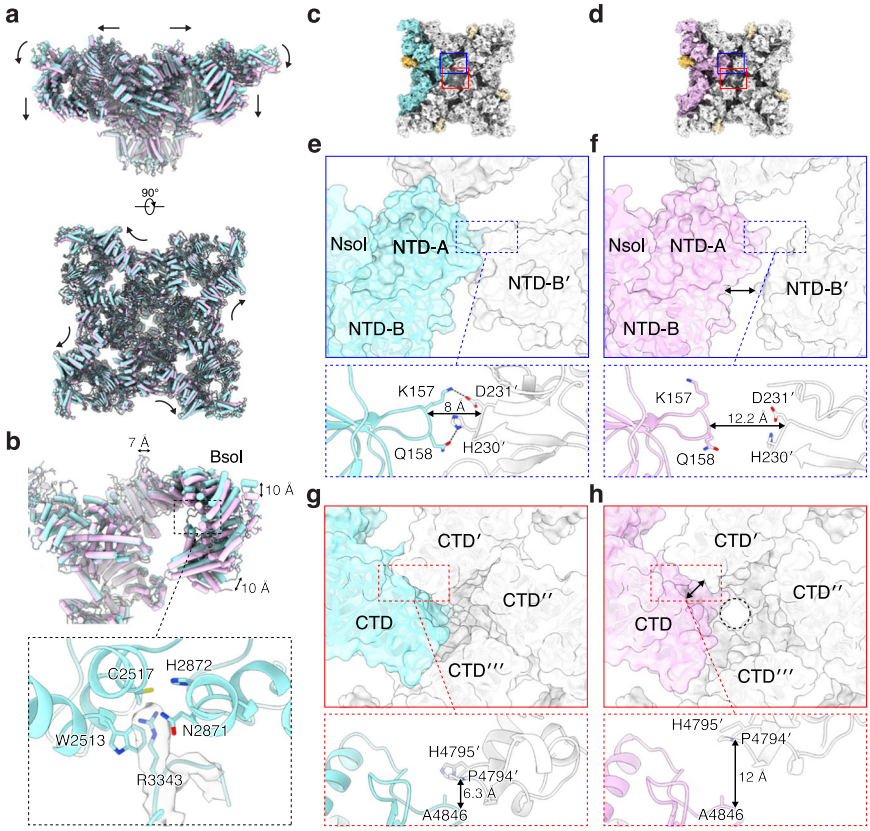

Fig. 2 | Global conformational changes between closed and open states of RyR3. a Structural overlay of closed (*cyan*) and open (*pink*) RyR3 aligned by the TMD, showing an overall outward and downward movement of the cytosolic domains. *Upper panel*, membrane plane view. *Lower panel*, intracellular view facing the ER membrane. **b** Structural overlay of closed (*cyan*) and open (*pink*) RyR3 aligned by the Jsol domain, showing a downward movement of the Bsol domain. A close-up view shows intra-subunit contact in the Bsol is mediated by an arginine residue in an extended loop. Cryo-EM density of the extended loop is shown (contour level = 0.05). Overall structure of **c** closed and **d** open state RyR3 viewed from the intracellular side with one subunit colored. N-terminal domains contact site between two subunits of **e** closed and **f** open state RyR3. Increased distance between NTD-A and NTD-B′ is observed upon channel opening. CTD contact site between two subunits of **g** closed and **h** open state RyR3. Widened gap between two CTD protomers is observed upon channel opening.

relative positions of NTD-A and NTD-B within a subunit appear identical, in agreement with the more extensive interactions found between these domains.

Immediately downstream of the last transmembrane region (S6) is a C-terminal domain (CTD) containing a Zn^{2+}-finger motif. In the closed state, the CTDs from all four subunits form a continuous ring with van der Waals interactions between Ala4846 and Gly4847 on one subunit, and residues 4792′–4794′ on a neighboring subunit (Fig. 2g). In the open state of the channel, these interactions are lost, with a substantial gap between the CTDs (Fig. 2h). These represent relative movements of 6 Å as measured by the Cα-Cα distances between Ala4846 and Pro4794′ of a neighboring subunit. Breaking these inter-subunit interactions likely provides an energetic barrier for channel opening.

Conformational changes in pore-forming domain upon channel opening

The pore-forming domain is formed by the S5 and S6 helices of all four subunits (Fig. 3a, b). The ion-conduction pathway is lined with many conserved residues that likely facilitate Ca^{2+} coordination and permeation. In the closed state, the hydrophobic gate is formed by Ile4759 from all four subunits, resulting in a pore radius of less than 1 Å, thereby inhibiting Ca^{2+} conduction (Fig. 3c). In the open state, the narrowest points are formed by Gly4716 and Gln4755, but with a minimum pore radius of ~3 Å that permits ion conduction. Upon channel opening, the S5 and S6 helices move outward, resulting in an increased distance from 10.6 Å to 18.2 Å as measured by the Cα distance between Ile4759 of diagonally opposed subunits (Fig. 3d, e; Supplementary Movie 2).

Binding sites for Ca^{2+}, caffeine, and ATP

In the RyR3 map obtained under activating conditions, we observed an unambiguous density for Ca^{2+}, at an interface between two domains that are not adjacent in sequence: the central solenoid (Csol) and C-terminal domain (CTD) (Fig. 4a, b). The Ca^{2+} ion is coordinated by the side chains of Glu3732 and Glu3806 in the Csol, and the Thr4823 carbonyl oxygen in the CTD. Binding of Ca^{2+} to this region causes a relative decrease in the distance between these two domains (Supplementary Movie 3). This causes a pivoting motion of the CTD, which is then translated to the associated S6 helices, thereby affecting channel gating.

We also observed excellent density for caffeine, whose binding site is formed by 4 different regions: a cytosolic extension of the loop connecting transmembrane helices S2 and S3, the CTD, the thumb-and-forefinger (TaF) domains, and a helix extending from the Csol. Binding of caffeine is obstructed by Trp4539, whose side chain swings out to make place (Fig. 4c; Supplementary Movie 4). The extended S2-S3 loop moves away by 2.5 Å relative to the CTD to make space, whereas the Csol helix containing Phe3598 moves closer by ~8 Å to participate in caffeine binding.

Excellent density is visible for ATP adjacent to the CTD, the extended S6 transmembrane helix, and the TaF domain (Fig. 4d). Several structural changes can be perceived in the binding pocket comparing open and closed RyR3 (Fig. 5; Supplementary Movie 5). In

https://doi.org/10.1038/s41467-024-52998-9

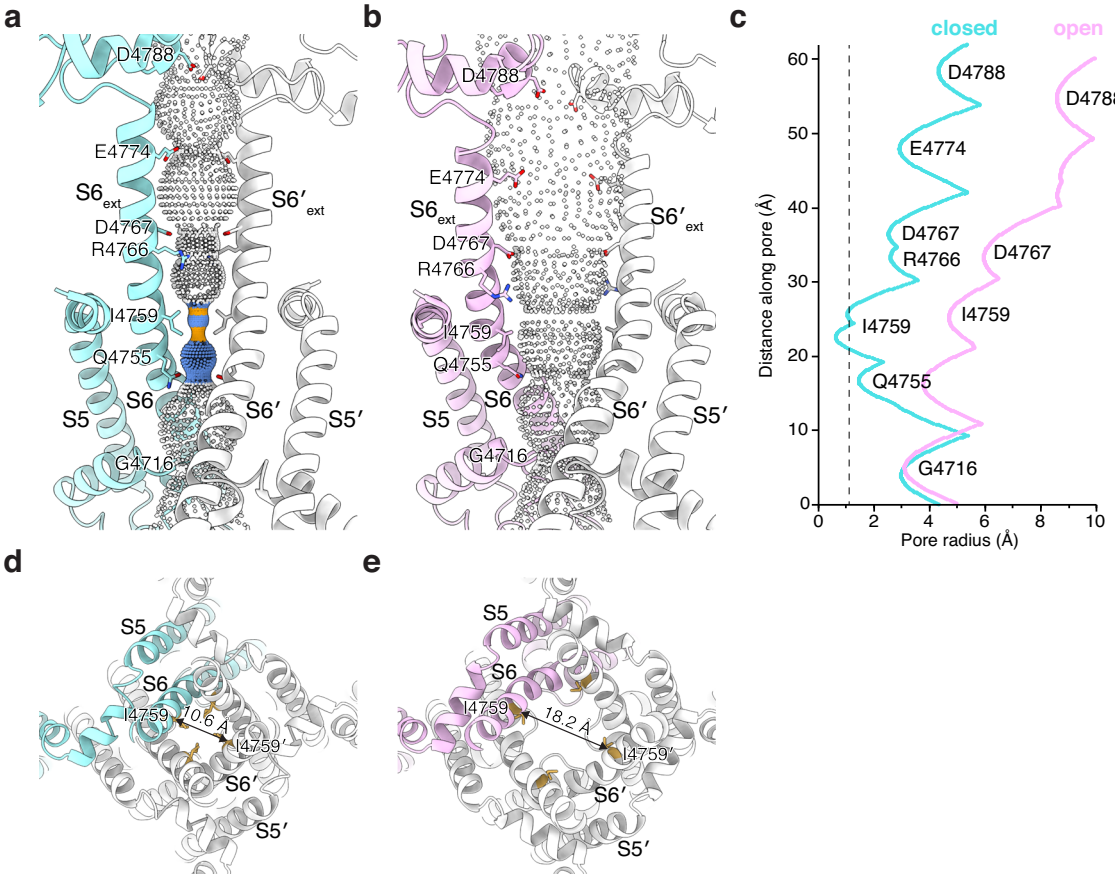

Fig. 3 | Pore-forming domain of RyR3 in closed and open states. Pore-forming domain of the **a** closed and **b** open state RyR3 viewed from the membrane plane. Only two out of four subunits are shown, and one shown in color. The dots are colored according to pore radii calculated using HOLE[73]: less than 1.15 Å (*orange*), 1.15 to 2.3 Å (*blue*), and greater than 2.3 Å (*white*). **c** Pore radii along the permeation path for closed (*cyan*) and open (*pink*) state of RyR3, calculated using HOLE[73]. The vertical dash line marks the radius of a dehydrated calcium ion at 1.1 Å[76]. Cross-sectional view of the pore-forming domain of **d** closed and **e** open state RyR3 viewed from the intracellular side. The Cα distance between two Ile4759 residues on opposite protomers are shown.

closed RyR3, Arg4054, located in the TaF domain, is part of a salt bridge network that involves Glu4051 (also in the TaF domain), which in turn links to Lys4643 in the S4-S5 linker (Fig. 5a). In the open RyR3, the S4-S5 linker has shifted, and Lys4643 is no longer involved in the salt bridge network. Arg4054 is now involved in ionic interactions with the ATP γ-phosphate, whereas Glu4051 now interacts with another Lys residue (Fig. 5b). When one also takes intersubunit contacts into account, in the closed state of the channel the ATP β-phosphate group would be close (~3.5 Å) to Glu4066′ of a neighboring subunit, likely providing some electrostatic repulsion (Fig. 5c). In the open state, Glu4066 is much further away, relieving the repulsion (Fig. 5d).

We note that these changes around ATP are not due to ATP alone but are observed when comparing open and closed channels. Indeed, previous structures of other RyR isoforms have shown that addition of ATP alone yields mostly closed channels[40,43]. However, different electrostatic interactions that involve ATP do help explain why this ligand helps favor the open state when other activating ligands are also present[40].

Ligand binding in the NTD

The N-terminal region is built up by the NTD-A and NTD-B domains, and the N-terminal solenoid (Nsol) (Fig. 1c, d). We observed a density compatible with a chloride anion, at the interface where these three domains meet (Fig. 6a, b). This putative chloride is stabilized by four different arginine residues. Without it, one would expect significant electrostatic repulsion due to these arginine residues, likely resulting in relative movements of these three domains that may alter channel gating. In RyR1, one of the arginines is replaced by a histidine (Fig. 6c; Supplementary Fig. 3). This likely explains the absence of chloride binding in both crystal structures and cryo-EM structures of RyR1[40,44,45]. RyR2 does contain four arginines at this interface (Fig. 6d; Supplementary Fig. 3), but a corresponding chloride ion has not been assigned in any RyR2 cryo-EM structure to date. One crystal structure of the isolated RyR2 N-terminal region has unambiguously shown the presence of a chloride anion in this area[46]. Closer inspection of available cryo-EM maps of RyR2 does show density compatible with a chloride ion, suggesting that this is a feature that distinguishes RyR2 and RyR3 from RyR1.

Unexpectedly, we observed density for another ATP molecule at the interface between the NTD-A and NTD-B domains (Fig. 6a, e). The adenine ring fits in a mostly hydrophobic pocket, but with an additional hydrogen bond mediated by Arg285 in the NTD-B domain. The β and γ phosphate groups are engaged in H-bond interactions, with an additional ionic interaction between the γ phosphate and Lys35 in NTD-A. This density has not been previously observed or reported in cryo-EM structures of RyR1 or RyR2 determined in presence of ATP (Fig. 6f, g). The ability of RyR3 to bind ATP in this region is likely a unique feature of RyR3. His205 involved in coordinating β phosphate of ATP is mutated to an asparagine and alanine in RyR1 and RyR2, respectively (Supplementary Fig. 3). Additional differences between RyR3 and RyR2 include substitution of RyR3 Ala56 by Ser in RyR2, likely introducing steric hindrance. RyR3 Ser272, which interacts with the β phosphate, is replaced by Ala in RyR2. Comparing the binding pocket for ATP in the open and closed RyR3, there are only subtle differences

https://doi.org/10.1038/s41467-024-52998-9

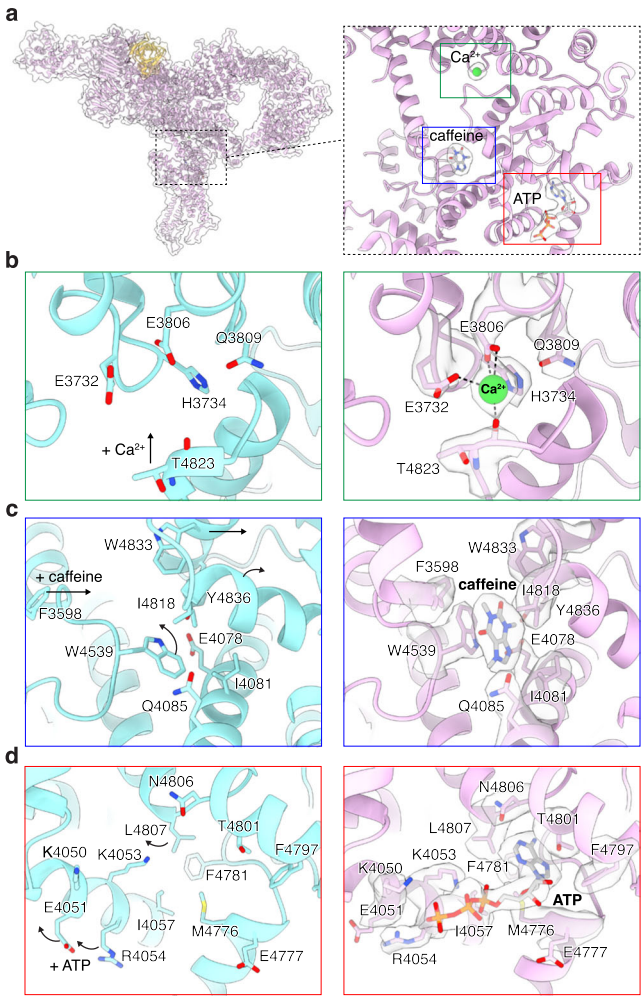

Fig. 4 | Conformational changes upon binding of activating ligands. a A single subunit of open state RyR3 (*pink*) bound to FKBP12.6 (*yellow*) with a close-up view of the ligand-binding sites. **b** Structural comparison of calcium binding site in closed (*left*) and open (*right*) state RyR3. The two structures are superimposed relative to Csol domain (residues 3637–3776). Ca^{2+} ion is shown as a green sphere along with corresponding cryo-EM density (contour level = 0.42). The arrow indicates the conformational change upon calcium binding. **c** Structural comparison of caffeine binding site in closed (*left*) and open (*right*) state RyR3. The two structures are superimposed relative to the S2-S3 linker region in TMD (residues 4489–4568). Caffeine is depicted as sticks with corresponding cryo-EM density (contour level = 0.27). Arrow indicates conformational change upon caffeine binding. **d** Structural comparison of the ATP binding in closed (*left*) and open (*right*) state RyR3. The two structures are superimposed relative to CTD (residues 4777 – 4815). ATP is depicted as sticks with corresponding cryo-EM density (contour level = 0.07). Arrow indicates conformational change upon ATP binding.

in sidechain conformations, suggesting that either state is compatible with ATP binding. Its binding at the NTD-A:NTD-B interface may confer structural rigidity. This ATP molecule is 81 Å away from the one bound to CTD (Supplementary Fig. 4). Whereas direct coupling between ATP binding at both sites is thus unlikely, it is possible that they influence one another's binding through long-range allosteric effects.

In open-state structures of RyR1 and RyR2, the local resolution of the NTD-A and NTD-B domains is frequently lower, indicating higher relative mobility. Binding of both chloride and ATP may prevent this, contributing to the high local resolution of this area in open RyR3 (Supplementary Fig. 2) and also indirectly affecting channel gating. Indeed, post-translational modifications and mutations at the interfaces between the N-terminal domains can allosterically affect channel opening[47], via a mechanism that links these to changes at the NTD-A:NTD-B′ across subunits, or to altered interactions between the NTDs and the central solenoid (Csol)[45,46,48]. Thus, the rigidity induced by binding of two ligands in this area may also have effects on channel gating.

Isoform-specific differences

RyR3 has been found to have a higher Po compared to RyR1 and RyR2 in various conditions[25–28]. In addition to the chloride and ATP binding sites in the N-terminal region, we note several other differences between RyR3 and the other isoforms.

FKBP12 and FKBP12.6 (FK506-binding proteins of 12 and 12.6 kDa, respectively) associate with RyRs, stabilizing their closed state[49]. It was previously noted that RyR3 has a lowered affinity for these proteins[50]. We used a GST-FKBP12.6 fusion protein to purify RyR3, indicating that it still retains binding. However, we observed weaker density for FKBP12.6 in our closed RyR3 structure (Fig. 1a), suggesting a reduced occupancy or higher relative mobility. In contrast, the FKBP12.6 density in the open RyR3 was better defined. A careful comparison of the FKBP12.6:RyR3 and FKBP12.6:RyR1 interfaces shows that there are various distinct differences that explain a lower affinity (Fig. 7a, b). In RyR1, His1300 in the SPRY3 domain interacts with Gln32 in FKBP12.6, but in RyR3 this is replaced by Ser1299, which no longer interacts. Lys36 in FKBP12.6 hydrogen bonds with Asn636 in the RyR1 SPRY1 domain, but this has been replaced by the bulkier Arg634 in RyR3, which cannot form a hydrogen bond due to steric hindrance and electrostatic repulsion. Val91 in FKBP12.6 forms van der Waals interactions with Ser1687 in the RyR1 junctional solenoid (Jsol) but has been replaced with Gly1582 in RyR3. These differences likely underlie the reduced affinity of FKBP12.6 for RyR3.

The cryo-EM density in the Bsol domain, particularly in the later portion, appears to be more resolved compared to existing RyR2 structures[41,51] (Supplementary Fig. 5a, b). Sequence alignment in this region reveals a 12-residue insertion in RyR2 that is absent in RyR1 and RyR3 near the end of the Bsol domain (Supplementary Fig. 5c). This insertion may contribute to the longer linker connecting the Bsol and Csol domains in RyR2. As a result, the Bsol domain in RyR2 is less constrained, possibly leading to higher conformational heterogeneity and lower visibility.

Several cryo-EM structures of RyR1 have revealed an additional transmembrane segment that precedes the S1 helix in sequence[40,52,53]. This helix makes contacts with helices S1 and S4 of one subunit, and S5′ of another subunit (Fig. 7c, d). We did not observe density for the S0 helix in our RyR3 structures, although the proposed sequence is largely conserved. In RyR1, Val4339 in S0 is juxtaposed with Val4820 at the end of S4, but both of these are replaced by Phe in RyR3, which would create a steric clash. Therefore, the S0 helix is likely more flexible in RyR3.

Disease-associated variants

To date, more than 1200 RyR3 sequence variants, found in patients with different disorders, have been reported in the ClinVar database[54]. Around 75% of these have been associated with epileptic encephalopathy, an epileptic condition that leads to cerebral dysfunction[55,56]. Supplementary Table 3 summarizes RyR3 mutations, reported in peer-reviewed literature and found in patients with a wide range of disorders. Mapping these onto the RyR3 structure (Fig. 8a) shows that most of these are found in the SPRY domains and in the Bsol region. A total of 10 of these mutations affect residues buried within the structures and are thus more likely to change function (Supplementary Table 3). For residues that are solvent exposed, a change in function is less likely.

We investigated sequence variants at the ligand binding sites. So far, no variants reported in peer-reviewed literature are at these binding sites, but 7 variants, linked to epileptic encephalopathy in ClinVar database, are found in the binding sites for ATP and chloride

https://doi.org/10.1038/s41467-024-52998-9

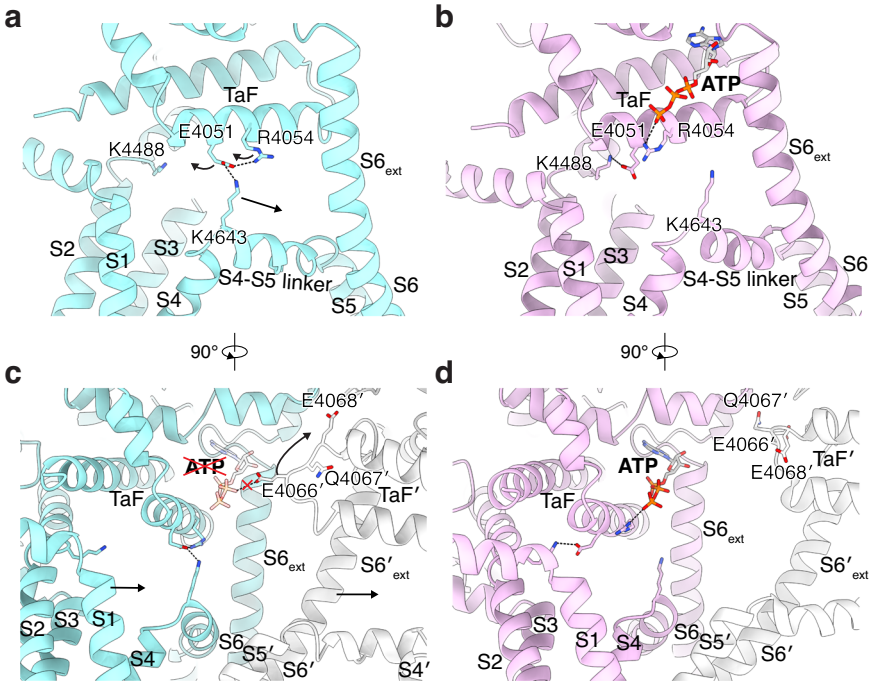

Fig. 5 | Proposed mechanism of channel activation by ATP binding. Close-up view of the ATP-binding region for **a** closed and **b** open state RyR3. The interactions of Glu4051 with Arg4054 and Lys4643 are disrupted upon binding ATP, effectively destabilizing the closed conformation. **c**, **d** Rotated views of (**a**, **b**), respectively. Electrostatic repulsion between ATP and Glu4066 of a neighboring subunit (*white*) are likely to disfavor ATP-binding in the closed conformation of the channel.

within the N-terminal region (Supplementary Table 4; Fig. 8b, c). Of note, mutation of arginine residues coordinating the chloride ion in RyR2 have been firmly linked to catecholaminergic polymorphic ventricular tachycardia (CPVT)[47,57]. For example, functional experiments on the RYR2 R420Q and R420W mutation, equivalent to RyR3 R412W, have indicated a gain-of-function phenotype[58,59]. Knock-in mice and hiPSC-derived cardiomyocytes with the RyR2 R420Q mutation recapitulate the CPVT phenotype and show structural alterations[59]. Crystallographic investigation of these mutations in the N-terminal disease hot spot have shown a change in the relative domain orientations[46]. Thus, it is very likely that the equivalent R412W mutation in RyR3 also introduces a gain-of-function and may be causative for epileptic encephalopathy. Knock-in mouse studies will be needed to investigate this further.

Discussion

We sought to elucidate the structure of RyR3, and solved cryo-EM structures in different experimental conditions. Surprisingly, we found that adding a cocktail of activating ligands (caffeine, ATP, and 30 μM free Ca^{2+}) led to a homogeneous population of only open channels, in stark contrast with studies with the RyR1 where a mixture of open and closed channels is observed under such conditions[40]. This indicates an intrinsically higher open probability for RyR3 than for RyR1. This matches previous functional experiments that have indicated an increased sensitivity of RyR3 to activating ligands and a higher maximum open probability[25–28], but we note that cryo-EM studies of RyR2 in the presence of activating ligands have also exclusively shown open channels[51,60].

What might be the cause for this increased open probability? The main sequence differences between the three RyR isoforms are located in the divergent regions (DR1–DR3), large areas that are intrinsically disordered[1]. Of note, DR2 is contained within a flexible loop of the SPRY3 domain and is almost non-existent for RyR3 (Supplementary Data 1). Although these regions likely impart distinct functional changes, they have not been visualized in any cryo-EM structure of RyRs to date, and thus may have little impact on the proportion of open isolated RyRs observed in the cryo-EM conditions. However, the DRs likely confer further isoform-specific difference in physiological context, where many additional binding partners are present.

Several differences in the RyR3 structure may explain its unique functional properties, including several sequence changes that are predicted to lower the affinity for FKBP12 and FKBP12.6. The latter proteins are known to bind RyR1 and RyR2 with high affinity and are thought to stabilize the closed state[49,61]. Despite the sequence changes in the binding site, RyR3 clearly has not lost its ability to associate with FKBPs, since the initial purification step included GST-FBKP12.6 as a bait protein (see methods). We did notice a decreased occupancy for FKBP12.6 in our closed RyR3 structure, suggesting that some was lost during the subsequent purification step. It is unclear why this was more pronounced for the closed state structure but is in agreement with previous observations that RyR3 binds FKBPs with lower affinity[50].

We also found the ligand profile to differ. RyR3 retains the previously identified binding sites for caffeine, ATP and activating Ca^{2+}, but an additional ATP binding site is found at the interface between the NTD-A and NTD-B domains, where it may confer rigidity and stabilize the relative domain orientation. This site is likely unique for RyR3 as it has not been observed before for RyR1 or RyR2, and there are differences in the residues that make up the binding pocket. We also identified a putative chloride anion at the interface between the NTD-A, NTD-B and Nsol domains. It is coordinated by arginine residues, all of which are conserved in RyR2, but not RyR1. Previous experiments with RyR2 have shown that mutation of a single arginine is sufficient to obliterate chloride binding to this site[46] and has been linked to CPVT[58].

The relationship between RyRs and disease has been firmly established for both RyR1 and RyR2. Through many functional experiments and knock-in mouse models, it is very clear that many sequence variants cause a gain- or loss-of-function phenotype, causing CPVT or cardiomyopathy (RyR2) or malignant hyperthermia, central core disease, or other myopathies (RyR1)[47,62]. A plethora of sequence variants have been identified for RyR3, including hundreds that have been found in patients with epileptic encephalopathy. Although the large number suggests a causative link, this

https://doi.org/10.1038/s41467-024-52998-9

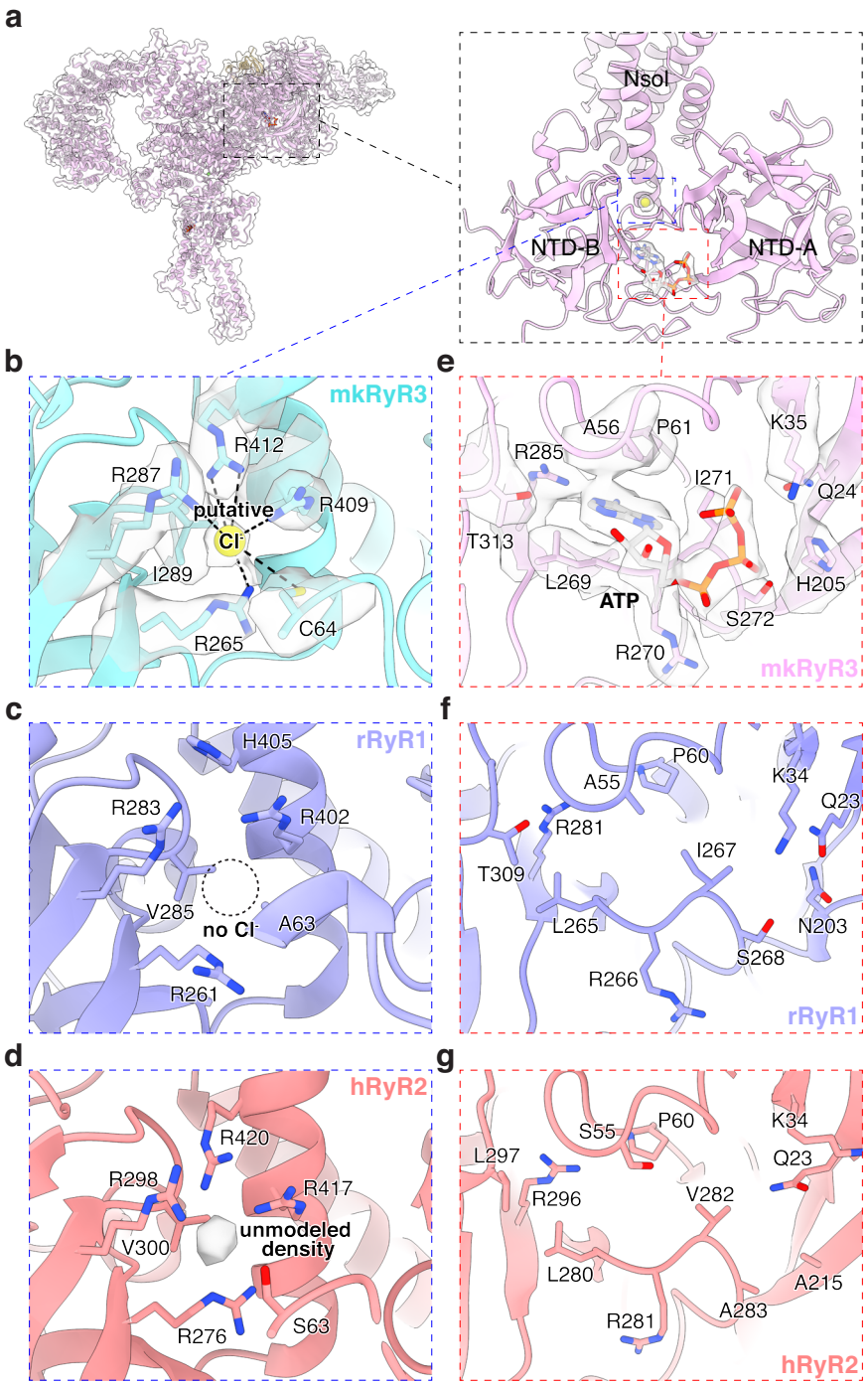

Fig. 6 | Structural basis of ATP and chloride binding in the N-terminal domains. **a** A single subunit of open state RyR3 (*pink*) bound to FKBP12.6 (*yellow*) with a close-up view of the ligand-binding sites in the N-terminal domains. Close-up view of the putative chloride-binding site in closed state **b** mink RyR3 (this study), **c** rabbit RyR1 (PDB: 7TZC), and **d** human RyR2 (PDB: 7U9T). Cl^- ion is shown as a yellow sphere with corresponding cryo-EM density (contour level = 0.08). An unmodelled cryo-EM density (contour level = 0.13) is observed at the putative chloride-binding site in hRyR2. Close-up view of the N-terminal domain ATP-binding site in open state structures determined in presence of ATP for **e** mink RyR3 (this study), **f** rabbit RyR1 (PDB: 5TAL), and **g** human RyR2 (PDB: 7UA9). ATP is depicted as sticks with corresponding cryo-EM density (contour level = 0.06).

remains to be proven. However, comparing known causative mutations in other isoforms suggests that at least a subset of the RyR3 variants may alter function, and thus also cause disease. For example, the R420Q and R420W mutations in RyR2 cause a gain-of-function phenotype and are causative of CPVT. They both affect the binding of chloride to the RyR2 N-terminal region and cause a relative reorientation of the N-terminal domains[46]. An equivalent mutation in RyR3 (R412W) has been found in a patient with epileptic encephalopathy and is thus likely to have similar structural and functional consequences.

Of note, many single nucleotide polymorphisms in RyR3 are located in intronic regions. They are less likely to directly affect the function of the individual RyR3 but may have an impact on the total amount of RyR3 protein. Since RyR3 inherently has a much higher open probability, disturbing the balance between RyR3 and the other isoforms thus presents another mechanism for an overall gain-of-

https://doi.org/10.1038/s41467-024-52998-9

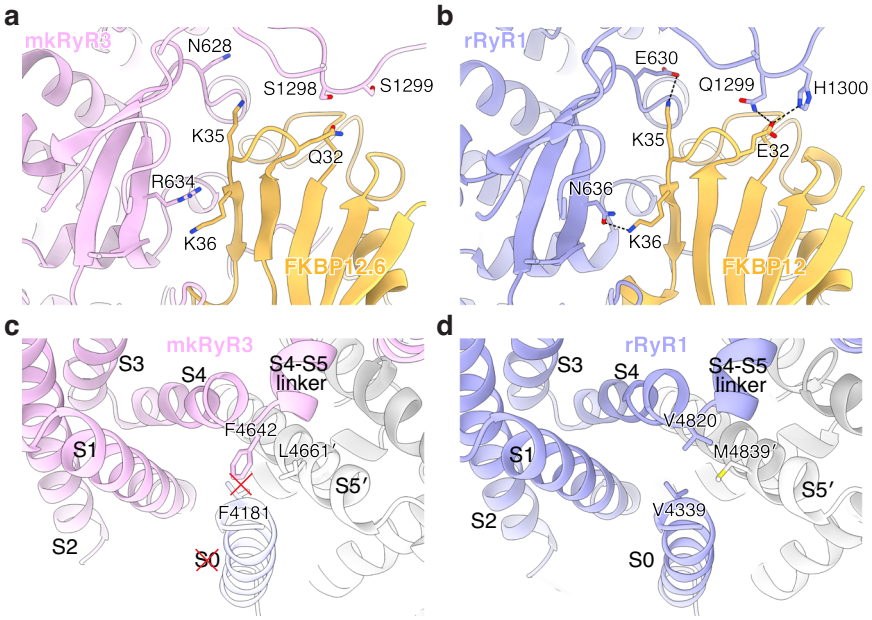

Fig. 7 | Isoform-specific differences between RyR3 and RyR1. Close-up view of the FKBP12.6 binding site for open state **a** mink RyR3 and **b** rabbit RyR1 (PDB: 7TZC). Close-up view of the S0 binding site for open state **c** mink RyR3 and **d** rabbit RyR1 (PDB: 8DVE). Substitution of two valines in RyR1 to bulkier phenylalanines in RyR3 near the S0 binding site likely prohibits binding of S0 helix in RyR3.

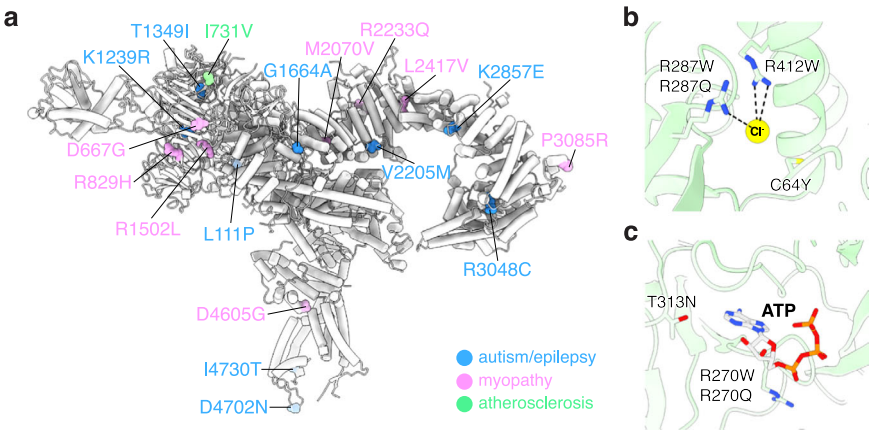

Fig. 8 | Structural mapping of disease-associated variants in RyR3. a Disease-associated variants mapped onto the structure of a single subunit of open state RyR3. The associated residues are shown as spheres and colored by disease associations: autism and epilepsy (*blue*), myopathy (*magenta*), and atherosclerosis (*green*). See Supplementary Table 3 for more details on the disease variants. Homology model of human RyR3 showing locations of disease-associated variants in the **b** putative chloride binding site and **c** N-terminal ATP-binding site. Cl^- ion and ATP are depicted as a yellow sphere and sticks, respectively. See Supplementary Table 4 for more details on the disease variants.

function. Whether RyR3 mutations truly cause disease remains to be demonstrated, and thus it will be of interest to generate animal models of several different RyR3 sequence variants to test for the role of RyR3 in disease.

Methods

Expression and purification of His-GST-FKBP12.6

We used a human FKBP12.6 (2–108) with an N-terminal His6-GST-TEV-tag[52]. The construct was transformed into *E. coli* strain Rosetta (DE3). Cells were grown in auto-induction media[63] at 37 °C to an optical density of 1, at which the temperature was changed to 20 °C and left shaking overnight. The cell pellet was obtained by centrifuging at 5000 × *g* for 20 min. The pellet was re-suspended in lysis buffer (50 mM HEPES pH 7.5, 500 mM NaCl, 5% glycerol, 5 mM BME) supplemented with 10 µg/mL DNAse I, 1 mM $MgCl_2$, 0.1 mg/mL lysozyme, 0.5 mM PMSF, and 5 mM imidazole. Cells were lysed by sonication. Cellular debris was removed by centrifugation at 44,000 × *g* for 45 min at 4 °C. The supernatant was loaded onto Ni-NTA resin (Qiagen) by batch binding, and incubated with gentle shaking for 30 min at 4 °C. The resin was washed with lysis buffer containing 30 mM imidazole and eluted with lysis buffer containing 500 mM imidazole. The protein was dialyzed overnight in buffer A (10 mM Tris pH 8.8, 10 mM NaCl, 5 mM BME), and applied onto an HiLoad 16/10 Q Sepharose High Performance column (Cytiva) equilibrated with buffer A and eluted using a linear gradient of buffer B (10 mM Tris pH 8.8, 1 M NaCl, 5 mM BME). The protein was further purified by size exclusion chromatography on a HiLoad 16/600 Superdex 200 pg column (Cytiva) in FPLC buffer (20 mM HEPES pH 7.5, 250 mM NaCl, 1 mM TCEP). The final purified protein was concentrated to around 10 mg/mL (measured by NanoDrop), flash-frozen in liquid nitrogen, and stored at −70 °C for later use.

Expression of RyR3

We used HEK293T cells stably expressing mink RyR3[27]. The cells were cultured in 150-mm dishes with Minimum Essential Medium α (MEM α; Gibco Cat #12561056) supplemented with 10% heat-inactivated Fetal Bovine Serum (Gibco, Cat #12484028), 10,000 U/mL penicillin-streptomycin solution, and additional 2 mM L-glutamine at 37 °C with 5% CO_2. Cells were maintained in culture below passage 10 and positively selected with 800 μg/mL G418 if kept in continued culture for more than a month. Upon confluency, plates were placed on ice, and cells were washed with cold Dulbecco's Phosphate Buffered Saline (DPBS), harvested with a scraper, and centrifuged at 250 × *g* for 5 minutes at 4 °C. Centrifugation cycles were repeated until all cells from 50–100 plates were collected. The cell pellet was flash-frozen in liquid nitrogen and stored at −70 °C for later use.

Purification of RyR3

All steps were performed at 4 °C. Cell pellets from 100 dishes were thawed and re-suspended in buffer A (20 mM Tris-maleate pH 6.8, 75 mM NaCl, 10% sucrose, 1 mM DTT, 1:1000 of protease inhibitor cocktail (PIC; Millipore Sigma Cat# 539134)) and lysed by sonication. Cellular debris was removed by centrifugation at 4400 × *g* for 10 min. The supernatant was ultracentrifuged at 100,000 × *g* for 60 min. The membrane pellet was collected, flash-frozen in liquid nitrogen, and stored at −70 °C for later use. The membrane fraction after thawing was solubilized in buffer B (25 mM HEPES pH 7.5, 500 mM NaCl, 2 mM DTT, 1% GDN, 1:1000 of PIC for 1 h. The solubilized mixture was ultracentrifuged at 100,000 × *g* for 60 min. The supernatant was mixed with 5 mg of His-GST-FKBP12.6 and incubated for 1 h. Next, 1.5 mL of Glutathione Sepharose 4B resin (Cytiva) was added for 1 h. The resin was poured into a gravity column, washed with buffer C (25 mM HEPES pH 7.5, 200 mM NaCl, 2 mM DTT, 0.02% GDN, 1:1000 of PIC) and eluted with buffer D (75 mM HEPES pH 8, 200 mM NaCl, 2 mM DTT, 0.02% GDN, 1:1000 of PIC, 15 mM glutathione). The His-GST tag was removed by overnight incubation with 150 μg of Tobacco Etch Virus (TEV) protease. The mixture was incubated with 0.2 mL of TALON resin (Cytiva) for 30 min to capture His-GST and His-TEV. The gravity column flow-through was applied onto a 1-mL HiTrap Heparin HP column (Cytiva) equilibrated in buffer E (20 mM HEPES pH 7.5, 50 mM NaCl, 2 mM DTT, 0.02% GDN, 1:1000 of PIC, 5 mM EGTA) and eluted with Buffer E containing 500 mM NaCl. For the activating condition, buffer E contains a final free Ca^{2+} concentration of 30 μM, using a total of 2 mM EGTA, 5 mM ATP, and 5 mM caffeine instead of 5 mM EGTA. The total concentration of Ca^{2+} to obtain 30 μM free Ca^{2+} was calculated with Ca-EGTA Calculator TS v1.3[64] and the final free Ca^{2+} concentration was verified using a PerfectIon Combination Calcium Electrode unit (Mettler Toledo). The elution is concentrated to 100 μL then diluted with 150 μL of Buffer E, making final [NaCl] = ~250 mM. The elution is then concentrated to ~5 mg/mL (measured with Nanodrop), flash-frozen in liquid nitrogen, and stored at −70 °C.

Electron microscopy

Separate grids were prepared under non-activating and activating conditions, respectively. Holey gold grids (UltrAuFoil Au 300 mesh, R 1.2/1.3) were glow-discharged for 2 min. 2.5 μL of RyR3-FKBP12.6 sample (non-activating or activating condition) was applied, blotted for 3 s (blot force of 7 to 10) using ashless blotting paper (Whatman) and subsequently plunge-frozen in liquid ethane using a Vitrobot Mark IV (Thermo Fisher Scientific) at 4 °C and 100% humidity.

Cryo-EM grids were screened on a Glacios electron microscope operating at 200 kV and equipped with a Falcon 3 camera (Thermo Fisher Scientific). High-resolution data were collected with a Titan Krios G2 electron microscope operating at 300 kV and equipped with a Falcon 4i camera and a Selectris energy filter (Thermo Fisher Scientific). Microscope operations and data collection were carried out using EPU software (Thermo Fisher Scientific). Movies were gathered in super-resolution counting mode at a calibrated magnification of 130,000×, corresponding to 0.96 Å per physical pixel. For the non-activating dataset, a total dose of 50 $e^-/Å^2$ using a dose rate of 10.20 e^-/pixel/s was delivered to 1404 frames in EER format with a defocus range of −1 to −2 μm. For the activating dataset, a total dose of 50 $e^-/Å^2$ using a dose rate of 12.06 e^-/pixel/s was delivered to 1188 frames in EER format with a defocus range of −0.5 to −2 μm.

CryoEM data processing

Detailed schematics of the cryo-EM data processing pipeline for both non-activating and activating datasets are summarized in Supplementary Figs. 1 and 2, respectively. All steps were performed in cryoSPARC[65] (v. 4.3–4.4.1) unless otherwise indicated. Movies were patch motion-corrected and curated based on ice thickness, defocus values, contrast transfer function (CTF) resolution estimation (lower than 6 Å were kept), full-frame motion, astigmatism, and average intensity. Particle picking was carried out using both crYOLO[66] (v. 1.9.7) and template picker in cryoSPARC. Templates used in template picker were generated from 2D classification of crYOLO-picked particles. After two rounds of 2D classification, particles from both pipelines were combined, and duplicates were removed. The particles were further cleaned using iterative rounds of ab-initio reconstruction and heterogeneous refinement. A consensus refinement was performed using non-uniform refinement. Masked 3D classification was performed using a TMD mask (residues 4016–4859) to classify the various pore conformations. Particles with the same pore state were combined, processed with reference-based motion correction, and refined with non-uniform refinement with C4 symmetry imposed. Pixel calibration was performed by comparing real-space correlation with a crystal structure of the N-terminal domains of RyR1 (PDB: 2XOA). Local refinements were performed to improve local resolution using four separate masks. The first mask consists of the N-terminal, SPRY, and Repeat1&2 domains (residues 1–1616) + FKBP12.6. The second mask consists of the Jsol, Csol, and Bsol domains (residues 1617–2492, 3487–4015). The third mask contains the Bsol and Repeat3&4 domain (residues 2170–3462). The fourth mask contains the TMD (residues 4016–4859). The first three local refinements used C4-symmetry expanded particles while the fourth refinement used non-symmetry expanded particles with C4 symmetry imposed. The resulting locally refined maps were combined in ChimeraX[67] to generate a composite map. Fourier shell correlation (FSC) plots, orientation distributions and refinement statistics are presented in Supplementary Figs. 1 and 2 and Supplementary Table 1. Mask-corrected FSC curves were calculated based on the FSC = 0.143 criterion. The local resolution estimations for the entire channel and each of the locally refined maps were calculated using the FSC = 0.5 criterion. Cryo-EM density visualization was done in UCSF ChimeraX[67].

Model building and refinement

A model of human RyR3 predicted by AlphaFold[68] was manually docked into the composite map using ChimeraX[67]. The mismatched residues were manually changed to that of mink RyR3 in Coot[69], and the model was improved through iterative cycles of manual building in Coot[69] and real-space refinement in PHENIX[70]. For the Repeat1&2 domain, which showed weak cryo-EM density, crystal structures of human RyR3 Repeat1&2 domain (PDB: 6UHB & 6UHA) were rigid-body-docked into the composite maps of non-activating and activating datasets in ChimeraX[67], and mismatched residues were manually changed to that of mink RyR3 in Coot[69]. Structural model validation was performed using PHENIX[71] and MolProbity[72]. Validation statistics are summarized in Supplementary Table 1. Structural images were prepared with UCSF ChimeraX[67]. Quantification of the pore radius in Fig. 3 was calculated using HOLE[73].

Homology modeling of human RyR3

The homology model of human RyR3 was constructed with MODELER[74] (v. 10.5) using mink RyR3 structure as the template. The sequence alignment was performed using Clustal Omega[75].

Reporting summary

Further information on research design is available in the Nature Portfolio Reporting Summary linked to this article.

Data availability

Atomic coordinates of RyR3 have been deposited in the Protein Data Bank (PDB) with the following accession codes: 9C1E (non-activating) and 9C1F (activating). The composite, consensus, and four local refinement maps of closed state RyR3 (non-activating) have been deposited in the Electron Microscopy Data Bank (EMDB) with the following accession codes: EMDB-45116 [https://www.ebi.ac.uk/pdbe/entry/emdb/EMD-45116], EMDB-45035 [https://www.ebi.ac.uk/pdbe/entry/emdb/EMD-45035], EMDB-45107 [https://www.ebi.ac.uk/pdbe/entry/emdb/EMD-45107], EMDB-45108 [https://www.ebi.ac.uk/pdbe/entry/emdb/EMD-45108], EMDB-45109 [https://www.ebi.ac.uk/pdbe/entry/emdb/EMD-45109], and EMDB-45110 [https://www.ebi.ac.uk/pdbe/entry/emdb/EMD-45110]. The composite, consensus, and four local refinement maps of open state RyR3 (activating) have been deposited in the EMDB with the following accession codes: EMDB-45117 [https://www.ebi.ac.uk/pdbe/entry/emdb/EMD-45117], EMDB-45111 [https://www.ebi.ac.uk/pdbe/entry/emdb/EMD-45111], EMDB-45112 [https://www.ebi.ac.uk/pdbe/entry/emdb/EMD-45112], EMDB-45113 [https://www.ebi.ac.uk/pdbe/entry/emdb/EMD-45113], EMDB-45114 [https://www.ebi.ac.uk/pdbe/entry/emdb/EMD-45114], and EMDB-45115 [https://www.ebi.ac.uk/pdbe/entry/emdb/EMD-45115]. The following previously published PDB codes were used for comparison: 2XOA, 6UHA, 6UHB, 6UHE, 6UHH, 7TZC,7U9T, 5TAL, 7UA9, 8DVE. The source data underlying Supplementary Figs. 1a and 2a is provided as a Source Data file. Source data are provided with this paper.

References

1. Woll, K. A. & Van Petegem, F. Calcium-release channels: structure and function of IP(3) receptors and ryanodine receptors. *Physiol. Rev.* **102**, 209–268 (2022).
2. Hakamata, Y., Nakai, J., Takeshima, H. & Imoto, K. Primary structure and distribution of a novel ryanodine receptor/calcium release channel from rabbit brain. *FEBS Lett.* **312**, 229–235 (1992).
3. Lanner, J. T., Georgiou, D. K., Joshi, A. D. & Hamilton, S. L. Ryanodine receptors: structure, expression, molecular details, and function in calcium release. *Cold Spring Harb. Perspect. Biol.* **2**, a003996 (2010).
4. Torres, R. & Hidalgo, C. Subcellular localization and transcriptional regulation of brain ryanodine receptors. Functional implications. *Cell Calcium* **116**, 102821 (2023).
5. Mori, F., Fukaya, M., Abe, H., Wakabayashi, K. & Watanabe, M. Developmental changes in expression of the three ryanodine receptor mRNAs in the mouse brain. *Neurosci. Lett.* **285**, 57–60 (2000).
6. Murayama, T. & Ogawa, Y. Properties of Ryr3 ryanodine receptor isoform in mammalian brain. *J. Biol. Chem.* **271**, 5079–5084 (1996).
7. Hidalgo, C. & Paula-Lima, A. RyR-mediated calcium release in hippocampal health and disease. *Trends Mol. Med* **30**, 25–36 (2024).
8. Vega-Vasquez, I. et al. Hippocampal dendritic spines express the RyR3 but not the RyR2 ryanodine receptor isoform. *Biochem Biophys. Res Commun.* **633**, 96–103 (2022).
9. Balschun, D. et al. Deletion of the ryanodine receptor type 3 (RyR3) impairs forms of synaptic plasticity and spatial learning. *EMBO J.* **18**, 5264–5273 (1999).
10. Galeotti, N. et al. Different involvement of type 1, 2, and 3 ryanodine receptors in memory processes. *Learn Mem.* **15**, 315–323 (2008).
11. Matsuo, N. et al. Comprehensive behavioral phenotyping of ryanodine receptor type 3 (RyR3) knockout mice: decreased social contact duration in two social interaction tests. *Front, Behav. Neurosci.* **3**, 3 (2009).
12. Supnet, C., Grant, J., Kong, H., Westaway, D. & Mayne, M. Amyloid-beta-(1-42) increases ryanodine receptor-3 expression and function in neurons of TgCRND8 mice. *J. Biol. Chem.* **281**, 38440–38447 (2006).
13. Supnet, C., Noonan, C., Richard, K., Bradley, J. & Mayne, M. Up-regulation of the type 3 ryanodine receptor is neuroprotective in the TgCRND8 mouse model of Alzheimer's disease. *J. Neurochem.* **112**, 356–365 (2010).
14. Nakamura-Maruyama, E. et al. Ryanodine receptors are involved in the improvement of depression-like behaviors through electroconvulsive shock in stressed mice. *Brain Stimul.* **14**, 36–47 (2021).
15. Schmidt, G. et al. A fixed 20:1 combination of cafedrine/theodrenaline increases cytosolic Ca(2+) concentration in human tracheal epithelial cells via ryanodine receptor-mediated Ca(2+) release. *Sci. Rep.* **13**, 16216 (2023).
16. Tsai, S. H. et al. Knockdown of RyR3 enhances adiponectin expression through an atf3-dependent pathway. *Endocrinology* **154**, 1117–1129 (2013).
17. Lohn, M. et al. Regulation of calcium sparks and spontaneous transient outward currents by RyR3 in arterial vascular smooth muscle cells. *Circ. Res.* **89**, 1051–1057 (2001).
18. Chang, Y. C. et al. Genome-wide linkage analysis and regional fine mapping identified variants in the RYR3 gene as a novel quantitative trait locus for circulating adiponectin in Chinese population. *Medicine* **95**, e5174 (2016).
19. Shendre, A. et al. RYR3 gene variants in subclinical atherosclerosis among HIV-infected women in the Women's Interagency HIV Study (WIHS). *Atherosclerosis* **233**, 666–672 (2014).
20. Shrestha, S. et al. Replication of RYR3 gene polymorphism association with cIMT among HIV-infected whites. *AIDS* **26**, 1571–1573 (2012).
21. Zhao, C. et al. Association of the RYR3 gene polymorphisms with atherosclerosis in elderly Japanese population. *BMC Cardiovasc. Disord.* **14**, 6 (2014).
22. Gong, S. et al. Polymorphisms within RYR3 gene are associated with risk and age at onset of hypertension, diabetes, and Alzheimer's disease. *Am. J. Hypertens.* **31**, 818–826 (2018).
23. Pergande, M. et al. The genomic and clinical landscape of fetal akinesia. *Genet. Med.* **22**, 511–523 (2020).
24. Dettling, M., Sander, T., Weber, M. & Steinlein, O. K. Mutation analysis of the ryanodine receptor gene isoform 3 (RYR3) in recurrent neuroleptic malignant syndrome. *J. Clin. Psychopharmacol.* **24**, 471–473 (2004).
25. Murayama, T. et al. Further characterization of the type 3 ryanodine receptor (RyR3) purified from rabbit diaphragm. *J. Biol. Chem.* **274**, 17297–17308 (1999).
26. Perez, C. F., Lopez, J. R. & Allen, P. D. Expression levels of RyR1 and RyR3 control resting free Ca2+ in skeletal muscle. *Am. J. Physiol. Cell Physiol.* **288**, C640–C649 (2005).
27. Rossi, D. et al. RyR1 and RyR3 isoforms provide distinct intracellular Ca^{2+} signals in HEK 293 cells. *J. Cell Sci.* **115**, 2497–2504 (2002).
28. Murayama, T. & Ogawa, Y. Characterization of type 3 ryanodine receptor (RyR3) of sarcoplasmic reticulum from rabbit skeletal muscles. *J. Biol. Chem.* **272**, 24030–24037 (1997).
29. Protasi, F. et al. RYR1 and RYR3 have different roles in the assembly of calcium release units of skeletal muscle. *Biophys. J.* **79**, 2494–2508 (2000).
30. Perez, C. F., Mukherjee, S. & Allen, P. D. Amino acids 1-1,680 of ryanodine receptor type 1 hold critical determinants of skeletal type for excitation-contraction coupling. Role of divergence domain D2. *J. Biol. Chem.* **278**, 39644–39652 (2003).

31. Perez, C. F., Voss, A., Pessah, I. N. & Allen, P. D. RyR1/RyR3 chimeras reveal that multiple domains of RyR1 are involved in skeletal-type E-C coupling. *Biophys. J.* **84**, 2655–2663 (2003).
32. Yang, D. et al. RyR3 amplifies RyR1-mediated Ca(2+)-induced Ca(2+) release in neonatal mammalian skeletal muscle. *J. Biol. Chem.* **276**, 40210–40214 (2001).
33. Conti, A., Gorza, L. & Sorrentino, V. Differential distribution of ryanodine receptor type 3 (RyR3) gene product in mammalian skeletal muscles. *Biochem. J.* **316**, 19–23 (1996).
34. Conti, A., Reggiani, C. & Sorrentino, V. Selective expression of the type 3 isoform of ryanodine receptor Ca2+ release channel (RyR3) in a subset of slow fibers in diaphragm and cephalic muscles of adult rabbits. *Biochem. Biophys. Res. Commun.* **337**, 195–200 (2005).
35. Eckhardt, J. et al. Extraocular muscle function is impaired in ryr3 (-/-) mice. *J. Gen. Physiol.* **151**, 929–943 (2019).
36. Nilipour, Y. et al. Ryanodine receptor type 3 (RYR3) as a novel gene associated with a myopathy with nemaline bodies. *Eur. J. Neurol.* **25**, 841–847 (2018).
37. Yuchi, Z., Lau, K. & Van Petegem, F. Disease mutations in the ryanodine receptor central region: crystal structures of a phosphorylation hot spot domain. *Structure* **20**, 1201–1211 (2012).
38. Sharma, M. R., Jeyakumar, L. H., Fleischer, S. & Wagenknecht, T. Three-dimensional structure of ryanodine receptor isoform three in two conformational states as visualized by cryo-electron microscopy. *J. Biol. Chem.* **275**, 9485–9491 (2000).
39. Liu, Z. et al. Three-dimensional reconstruction of the recombinant type 3 ryanodine receptor and localization of its amino terminus. *Proc. Natl. Acad. Sci. USA* **98**, 6104–6109 (2001).
40. des Georges, A. et al. Structural basis for gating and activation of RyR1. *Cell* **167**, 145–157.e17 (2016).
41. Miotto, M. C. et al. Structural analyses of human ryanodine receptor type 2 channels reveal the mechanisms for sudden cardiac death and treatment. *Sci. Adv.* **8**, eabo1272 (2022).
42. Melville, Z. et al. A drug and ATP binding site in type 1 ryanodine receptor. *Structure* (2022).
43. Cholak, S. et al. Allosteric modulation of ryanodine receptor RyR1 by nucleotide derivatives. *Structure* (2023).
44. Tung, C. C., Lobo, P. A., Kimlicka, L. & Van Petegem, F. The amino-terminal disease hotspot of ryanodine receptors forms a cytoplasmic vestibule. *Nature* **468**, 585–588 (2010).
45. Kimlicka, L., Lau, K., Tung, C. C. & Van Petegem, F. Disease mutations in the ryanodine receptor N-terminal region couple to a mobile intersubunit interface. *Nat. Commun.* **4**, 1506 (2013).
46. Kimlicka, L. et al. The cardiac ryanodine receptor N-terminal region contains an anion binding site that is targeted by disease mutations. *Structure* **21**, 1440–1449 (2013).
47. Pancaroglu, R. & Van Petegem, F. Calcium channelopathies: structural insights into disorders of the muscle excitation-contraction complex. *Annu. Rev. Genet* **52**, 373–396 (2018).
48. van den Bersselaar, L. R. et al. RYR1 variant c.38T>G, p.Leu13Arg causes hypersensitivity of the ryanodine receptor-1 and is pathogenic for malignant hyperthermia. *Br. J. Anaesth.* **127**, e63–e65 (2021).
49. Van Petegem, F. Ryanodine receptors: structure and function. *J. Biol. Chem.* **287**, 31624–31632 (2012).
50. Fessenden, J. D. et al. Divergent functional properties of ryanodine receptor types 1 and 3 expressed in a myogenic cell line. *Biophys. J.* **79**, 2509–2525 (2000).
51. Gong, D. et al. Modulation of cardiac ryanodine receptor 2 by calmodulin. *Nature* **572**, 347–351 (2019).
52. Ma, R. et al. Structural basis for diamide modulation of ryanodine receptor. *Nat. Chem. Biol.* **16**, 1246–1254 (2020).
53. Haji-Ghassemi, O. et al. Cryo-EM analysis of scorpion toxin binding to ryanodine receptors reveals subconductance that is abolished by PKA phosphorylation. *Sci. Adv.* **9**, eadf4936 (2023).
54. Landrum, M. J. et al. ClinVar: improvements to accessing data. *Nucleic Acids Res.* **48**, D835–D844 (2020).
55. Khan, S. & Al Baradie, R. Epileptic encephalopathies: an overview. *Epilepsy Res. Treat.* **2012**, 403592 (2012).
56. Kalser, J. & Cross, J. H. The epileptic encephalopathy jungle—from Dr West to the concepts of aetiology-related and developmental encephalopathies. *Curr. Opin. Neurol.* **31**, 216–222 (2018).
57. Medeiros-Domingo, A. et al. The RYR2-encoded ryanodine receptor/calcium release channel in patients diagnosed previously with either catecholaminergic polymorphic ventricular tachycardia or genotype negative, exercise-induced long QT syndrome: a comprehensive open reading frame mutational analysis. *J. Am. Coll. Cardiol.* **54**, 2065–2074 (2009).
58. Tang, Y., Tian, X., Wang, R., Fill, M. & Chen, S. R. Abnormal termination of Ca2+ release is a common defect of RyR2 mutations associated with cardiomyopathies. *Circ. Res.* **110**, 968–977 (2012).
59. Yin, L. et al. Impaired binding to junctophilin-2 and nanostructural alteration in CPVT mutation. *Circ. Res.* **129**, e35–e52 (2021).
60. Chi, X. et al. Molecular basis for allosteric regulation of the type 2 ryanodine receptor channel gating by key modulators. *Proc. Natl. Acad. Sci. USA* **116**, 25575–25582 (2019).
61. Brillantes, A. B. et al. Stabilization of calcium release channel (ryanodine receptor) function by FK506-binding protein. *Cell* **77**, 513–523 (1994).
62. Betzenhauser, M. J. & Marks, A. R. Ryanodine receptor channelopathies. *Pflug. Arch.* **460**, 467–480 (2010).
63. Studier, F. W. Protein production by auto-induction in high density shaking cultures. *Protein Expr. Purif.* **41**, 207–234 (2005).
64. Schoenmakers, T. J., Visser, G. J., Flik, G. & Theuvenet, A. P. CHELATOR: an improved method for computing metal ion concentrations in physiological solutions. *Biotechniques* **12**, 876–879 (1992). 870-4.
65. Punjani, A., Rubinstein, J. L., Fleet, D. J. & Brubaker, M. A. cryoSPARC: algorithms for rapid unsupervised cryo-EM structure determination. *Nat. Methods* **14**, 290–296 (2017).
66. Wagner, T. et al. SPHIRE-crYOLO is a fast and accurate fully automated particle picker for cryo-EM. *Commun. Biol.* **2**, 218 (2019).
67. Pettersen, E. F. et al. UCSF ChimeraX: structure visualization for researchers, educators, and developers. *Protein Sci.* **30**, 70–82 (2021).
68. Jumper, J. et al. Highly accurate protein structure prediction with AlphaFold. *Nature* **596**, 583–589 (2021).
69. Emsley, P., Lohkamp, B., Scott, W. G. & Cowtan, K. Features and development of Coot. *Acta Crystallogr. D Biol. Crystallogr* **66**, 486–501 (2010).
70. Afonine, P. V. et al. Real-space refinement in PHENIX for cryo-EM and crystallography. *Acta Crystallogr. D Struct. Biol.* **74**, 531–544 (2018).
71. Afonine, P. V. et al. New tools for the analysis and validation of cryo-EM maps and atomic models. *Acta Crystallogr. D Struct. Biol.* **74**, 814–840 (2018).
72. Williams, C. J. et al. MolProbity: more and better reference data for improved all-atom structure validation. *Protein Sci.* **27**, 293–315 (2018).
73. Smart, O. S., Neduvelil, J. G., Wang, X., Wallace, B. A. & Sansom, M. S. HOLE: a program for the analysis of the pore dimensions of ion channel structural models. *J. Mol. Graph* **14**, 376 (1996). 354-60.
74. Webb, B. & Sali, A. Comparative protein structure modeling using MODELLER. *Curr. Protoc. Bioinform.* **54**, 5 6 1–5 6 37 (2016).
75. Madeira, F. et al. Search and sequence analysis tools services from EMBL-EBI in 2022. *Nucleic Acids Res.* **50**, W276–W279 (2022).
76. Persson, I. Hydrated metal ions in aqueous solution: How regular are their structures? *Pure Appl. Chem.* **82**, 1901–1917 (2010).

Acknowledgements
This work is funded by Canadian Institutes of Health Research grant PJT-159601 (F.V.P.), Fonds de Recherche du Québec–Santé fellowship BF7-310936 (Y.S.C.), and Michael Smith Health Research BC Research Trainee award RT-2023-3133 (Y.S.C.). Cryo-EM grids were prepared and collected at the High Resolution Macromolecular Electron Microscopy (HRMEM) facility at the University of British Columbia (https://cryoem.med.ubc.ca). We thank Claire Atkinson, Joeseph Felt, Liam Worrall and Natalie Strynadka. HRMEM is funded by the Canadian Foundation of Innovation and the British Columbia Knowledge Development Fund.

Author contributions
F.V.P. and V.S. conceived the project. M.C. performed mammalian protein expression with guidance by D.R. for maintaining the stable cell line. Y.S.C. & M.G. prepared cryo-EM samples. Y.S.C. performed cryo-EM data processing, model building and refinement. Y.S.C. and F.V.P. analyzed the structures and wrote the first version of the manuscript, with edits provided by all other authors.

Competing interests
The authors declare no competing interests.

Additional information
Supplementary information The online version contains supplementary material available at https://doi.org/10.1038/s41467-024-52998-9.

Correspondence and requests for materials should be addressed to Filip Van Petegem.

Peer review information *Nature Communications* thanks Deshun Gong and Manjuli Sharma for their contribution to the peer review of this work. A peer review file is available.